Mass spectrometry and in situ x-ray photoelectron spectroscopy investigations of organometallic species induced by the etching of germanium, antimony and selenium in a methane-based plasma

T Meyer, A Girard, M Bouška, E Baudet, M Baillieul, P Němec, V Nazabal, C Cardinaud

Mass spectrometry and in situ X-ray Photoelectron Spectroscopy investigations of organometallic species induced by the etching of germanium, antimony and selenium in a methane-based plasma

T. Meyer[1], A. Girard[1], M. Bouška[2], E. Baudet[2], M. Baillieul[3], P. Němec[2], V. Nazabal[3] and C. Cardinaud[1]

[1] Université de Nantes, CNRS, Institut des Matériaux Jean Rouxel, IMN, F-44000 Nantes, France

[2] Department of Graphic Arts and Photophysics, Faculty of Chemical Technology, University of Pardubice, Studentskà 573, 53210 Pardubice, Czech Republic

[3] Univ Rennes, CNRS, ISCR (Institut des Sciences Chimiques de Rennes) – UMR 6226, F-35000 Rennes, France

[a)] electronic mail: christophe.cardinaud@cnrs-imn.fr

Abstract. Organometallic positive ions were identified in Inductively Coupled Plasmas by means of Mass Spectrometry (MS) during the etching of Ge, Sb, Se materials. A preliminary study was focused on identifying M_xH_y+ (M = Ge, Sb, Se) positive ion clusters during a H_2/Ar etching process. The methane addition to the H_2/Ar mixture generates CH_x reactive neutral species. The latter react with the metalloids within gas phase to form $M_xC_yH_z^+$ organometallic ions. In addition, the etching of Sb_2Se_3 and $Ge_{19.5}Sb_{17.8}Se_{62.7}$ bulk targets forms mixed products via ion-molecule reactions as evidenced by the presence of $SeSbC_xH_y^+$ ion clusters. Changes in surface composition induced by the newly formed organometallic structures were investigated using in situ X-ray Photoelectron Spectroscopy (XPS). In the case of the Ge and Sb surfaces, (M)-M-C_x environments broadened the Ge $2p_{3/2}$, Ge 3d, Sb 3d and Sb 4d spectra to higher values of binding energy. For the Se surface, only the hydrogen and methyl bonding could explain the important broadening of the Se 3d core level. It was found that the $Ge_{39}Se_{61}$ thin film presents an induced (Ge)-Ge-Se entity on the Ge $2p_{3/2}$ and Ge 3d core levels.

1. Introduction

The bonding of -at least- one atom of carbon and one atom of metal or metalloid (Si, Ge, As, Sb, Se, Te) defines a type of compounds known as organometals. The latter are formed via successive biochemical processes (*e.g.* methylation and demethylation)[1-4], synthesis[5] or gas phase reaction[6-8].

From the second half of the 20th century to the present time, Mass Spectrometry (MS) analysis became a suitable analytical technique to investigate the organometallic compounds regardless of their phase thanks to the development of soft ionization techniques as the electrospray ionization, fast atom bombardment and matrix-assisted laser desorption/ionization

[9-12]. Simultaneously, Inductively Coupled Plasma (ICP) has been exploited for the ICP-MS analysis, which has been also used to identify volatile organometallic compounds[13,14]. Broadly speaking, data processing is carried out using the isotopic distribution of the metal contained in the investigated sample. Nevertheless, the fragmentation of such compounds mostly depends on the ionization source, which may entangle the interpretation of the resulting spectrum.

Plasma etching and organometallic chemistry are two fields growing apart, hence no link is clearly established yet. However, during the etching of a metal-containing material, a methane-based plasma is an unusual source of organometallic compounds. A first way is the sputtering by ion bombardment, which ejects the metal from the surface, and subsequently the gas phase reactions generate organometallic compounds. The second way is from the chemical etching process. The latter is basically a two-step mechanism involving the successive adsorption of reactive neutral species (typically H and CH_x) and the desorption of a hydride or an organometallic etch product.

Methane-based plasmas have been used on metalloid-containing materials as ZnSe[15,16], GaAs[17], GaSb[17,18], InSb[19] and Ge-As-Se[20], aiming for patterned nanostructures. The etching processes of III-V and II-VI semiconductors were mostly focused on the etch rate and the imaging of patterned profiles. Few studies have been realized to understand the etching mechanisms combining plasma and surface diagnostics on HgCdTe[21], ZnSe[22], GaAs[23] , InP[24] materials. These authors demonstrated the formation of hydride and organometallic species during methane- based processes via mass spectrometry analysis. However, the investigation of the organogermanium ions is still let aside because halogen-based plasmas predominate the etching of Ge-containing materials. Besides, Sb and Se are not etched as pure elements, which is probably why the identification of organoantimony and organoselenium ions has not been performed yet.

The identification of etch products remains crucial to obtain a global overview of the etching process whether it is in the plasma, at the surface of an investigated material or on the reactor wall. Once the rate limiting step (nonvolatile species, lack of etchant, lack of ions, etc.) of a process is identified, the plasma chemistry can be subsequently optimized to enhance or reduce the kinetic formation of specific etch products. As the redeposit of etch products is an inevitable feature of the etching process, the knowledge of such information is also required to adapt the cleaning process.

The aim of this study is to understand the etching mechanisms of the Ge-Sb-Se ternary in methane-based plasma. In recent years, the related Ge-Sb-Se chalcogenide thin film has been patterned for photonic applications in halogen-based plasma[25-27]. Nevertheless, the study of Ge-Sb-Se material etching in methane-based plasmas is non- existent, hindering the establishment of such plasma chemistry. The critical prerequisite is to obtain basic information during and after the etching of the stoichiometric $GeSe_2$ and Sb_2Se_3 materials.

In this article, we identify the hydrides and the organometallic ion clusters formed during the etching of Ge, Sb and Se pure elements using H_2/Ar and CH_4/H_2/Ar. The results are systematically compared with those obtained from the fragmentation of $M_xC_yH_z$ (M = Ge, Sb, Se) stable organometallic compounds. This step is crucial for the subsequent interpretation of the mass spectra obtained during the etching of $GeSe_2$, Sb_2Se_3. In addition, we also investigate the nonvolatile organometallic compounds at the surface of a $Ge_{39}Se_{61}$ thin film, a Sb_2Se_3 powder and a $Ge_{19}Sb_{21}Se_{60}$ thin film by means of *in situ* XPS.

2. EXPERIMENTAL

For the present study, the identification of etch products is firstly performed using germanium (5N 100 mm wafer; Goodfellow), vitreous Se (4N pellet; Codex International) and Sb (1*2 cm ingot; HiChem SPOL S.R.O) to avoid the overlapping between different ion cluster

signals (*i.e.* $GeC_xH_y^+$ and $SeC_xH_y^+$). In addition, a Sb_2Se_3 bulk target (r = 2.5 cm), a $GeSe_2$ glass target (r = 2.5 cm), and a $Ge_{19.5}Sb_{17.8}Se_{62.7}$ glass target (2×1 cm²) were etched to identify other etch products. Surface analysis required thin samples (< 1 mm) to perform an *in situ* transfer and to limit an induced charging effect. That is why Sb and Sb_2Se_3 samples were run as powders prepared from bulk targets; and 1 μm thick $Ge_{39}Se_{61}$ and 1.5 μm thick $Ge_{19}Sb_{21}Se_{60}$ thin films were prepared by pulsed laser deposition by ablating a $GeSe_2$ glass target and a $Ge_{19.5}Sb_{17.8}Se_{62.7}$ glass target with an excimer laser operating at 248 nm. More details about glass target synthesis and the deposition process can be found in[28].

Hydrogen-based (H_2/Ar) and methane-based (CH_4/H_2/Ar) etching processes were performed in an ICP reactor. The etching vessel is composed of a plasma source and an etching chamber. The former consists of an alumina tube of 26 cm in height and 18 cm in diameter, with an external loop antenna. The source power is provided by a generator operating at 13.56 MHz (Dressler CESAR 1325) which is connected to the antenna via a matching box. The cylindrical etching chamber is 35 cm in diameter and 47 cm in height. Samples and targets are placed on a substrate at the center of the etching chamber. The substrate holder is located 24 cm below the antenna and can be biased using a variable power supply at 13.56 MHz. The sample holder receives Si wafers 100 mm in diameter that are clamped mechanically via an anodized aluminum ring. A cryostat ensures the temperature regulation of the sample holder. Between the wafer and the substrate holder, the heat exchange is obtained by a 10 mbar He static pressure at the wafer backside. In the present study, temperature regulation was fixed to 20 C. The partial pressures of hydrogen, argon and methane are controlled via mass flow controllers. Before each run, a conditioning procedure consists in a deposition process using a CH_4/H_2 plasma at 20 mTorr total pressure, 400 W source power and without bias. After the etching of Ge, Se and $GeSe_2$ and $Ge_{39}Se_{61}$ materials, the etching chamber is cleaned with a SF_6 plasma, whereas the cleaning is performed with a H_2/Ar plasma after the etching of Sb-containing materials. After plasma conditioning and cleaning, no fluorine and oxygen emission lines were detected when using optical emission spectroscopy.

A mass analyzer (Hiden analytical EQP 1000) was used to identify clusters of positive ions. The device consists of a combination of lenses, an energy filter, a quadrupole mass filter and a detector. At the entrance of the spectrometer, a lens can be negatively biased to attract the plasma positive ions which enter inside the mass spectrometer through a 100 μm in diameter aperture. The latter is positioned at 15 cm from the center of the chamber and 2 cm above the substrate holder. Then, the ion beam is focused in a transfer ion optics, in which the ions are accelerated to the input of the energy filter ε_{filter} (typically - 40 eV for positive ions). The ion beam is then focused in a 45 sector field energy analyzer thanks to a quadrupole lens. The energy filter is composed of one outer plate and inner plate biased at $\varepsilon_{filter} \pm 7.4$ V. At the end of the energy analyzer, ions are focused in the quadrupole mass filter according to their mass to charge ratio (m/z). In the detector, the ions strike the conversion dynode biased at - 1200 V, and the subsequent production of electrons triggers the secondary electron multiplier set at - 1800 V. Inside the mass spectrometer, the background pressure is 1×10^{-8} Torr. Ion transporting lenses are calibrated using Ar^+ (m/z 40). Spectra are recorded at the average ion energy of the Ar^+ ion energy distribution, although that for the etch products are slightly different. The multiple linear regression (MLR) analysis is an extensively used analytical method to predict an outcome on the basis of multiple independent variables. In our present study, MLR is applied to extract the contribution of each ion within a cluster by solving Eq. 1.

$$S = \alpha I + e \quad (1)$$

The vector S is the experimental data (*e.g.* the MS signals of $M_xC_yH_z^+$) delimited in a defined mass range; the vector α contains all the regression coefficients (α_1, α_2...); the matrix I contains the isotopic distribution of each ion (*i.e.* the independent variables) potentially involved in S; and e represents the residual (e_1, e_2...). Within a $M_xC_yH_z$ cluster, the lighter ion (z = 0) and the heaviest ion ($z = z_{max}$) delimit the number of ions contained in the matrix I by taking into account all ions from z = 0 to $z = z_{max}$. Starting from the theoretical abundance

pattern of $M_xC_y^+$, the isotopic distribution is shifted according to the number of H bonded. The purpose is to predict a spectrum S_p using the same matrix I with the estimated vector α_p as represented in Eq. 2.

$$S_p = \alpha_p I + e_p \qquad (2)$$

By combining the MLR analysis with the least-square method, the vector α_p is estimated from α such as the sum of the squared residuals $\sum(e - e_p)^2$ is minimized. The goodness of the fit is interpreted thanks to the coefficient of determination R^2 which is defined by the fraction of the variance explained by the model. A R^2 coefficient close to 1 indicates that S_p can be predicted with the set of regression coefficients (α_{p1}, α_{p2}...).

Chemical bonds at the sample surface are studied by *in situ* XPS. Photoelectron spectra are obtained using a monochromatic Al Kα X-ray source (hν = 1486.6 eV, SPECS XR 50 M and SPECS FOCUS 500) operating from 25 to 400 W according to the sample. All samples are transferred from the etching vessel to the XPS chamber via an Ultra High Vacuum (UHV) buffer chamber, preventing oxidation of the samples after etching.. This also ensures that the pressure inside the analysis chamber is always maintained below 3×10−8 mbar. Photoelectrons are analyzed according to their kinetic energy in a hemispherical analyzer (SPECS PHOIBOS HR 150). Spectra are acquired with a pass energy set at 14 eV and an energy step of 0.1 eV. An electron flood gun is systematically used to compensate for surface charging effects. The CASA-XPS software (Casa Software Ltd., UK) is used or data processing of the Ge $2p_{3/2}$, Sb 3d, C 1s, Se 3d, Sb 4d and Ge 3d core level spectra. The contribution of the inelastic background is modelled using a Shirley background[29]. Curve fitting is carried out using Gaussian-Lorentzian peak shapes (LF). Same peaks within a spin orbit doublet are assigned with the same Full Width at Half Maximum (FWHM), although independent doublets are affected with different FWHM values; spin-orbit splitting and area ratio are fixed according to

the literature[28] and NIST XPS database[30]. The energy calibration is performed using the (Ge)-Ge-Ge, (Sb)-Sb-Sb, (Ge)-Se-Ge and (Se)-Sb-Se chemical states which were retrieved from pristine samples using the C-H bond of the C 1s core level (binding energy, BE = 284.8 eV). Therefore, Ge and Sb spectra were calibrated according to the Ge-Ge (BE = 29.0 eV; Ge $3d_{5/2}$) and Sb-Sb (BE = 528.0 eV; Sb $3d_{5/2}$) chemical states, respectively. Since C 1s and Se $L_3M_3M_{4,5}$ overlap, selenide materials were calibrated assuming that (Ge)-Se-Ge environment (BE = 54.7 eV, Se $3d_{5/2}$) and (Se)-Sb-Se (*i.e.* [$SbSe_{3/2}$] unit) (BE = 529.0 eV, Sb $3d_{5/2}$) remain the dominant contribution after the etching process. These binding energy values are consistent with those reported in the NIST XPS database[30] as well as the studies concerning $GeSe_x$[31-34] and $SbSe_x$ materials[35-37]. As both (Se)-Ge-Se (Ge $2p_{3/2}$ and Ge 3d) and (Ge)-Se-Ge (Se 3d) bonding are not reliable on the etched Ge-Sb-Se thin film, the energy calibration is performed on the doublet at lower binding energy of the Sb 3d core level, assuming that this contribution is predominantly the [$SbSe_{3/2}$] unit.

3. Results and discussions

3.1. Mass spectrometry analysis

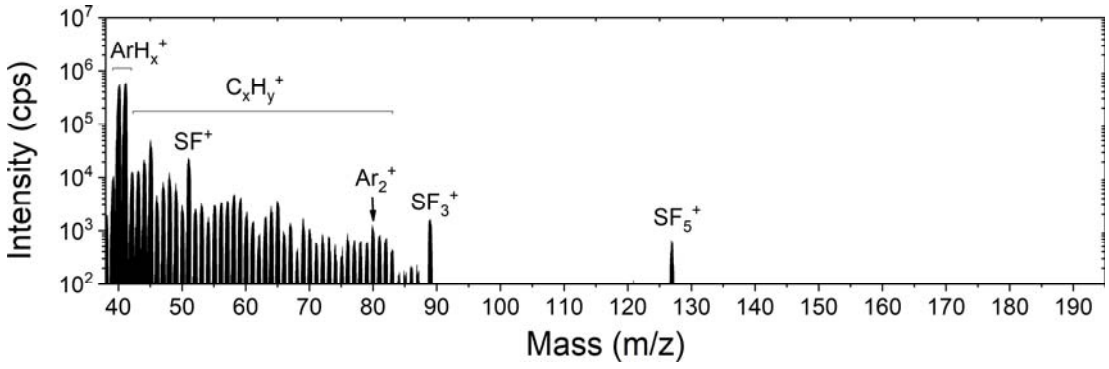

Figure 1: Reference spectrum (ion analysis) in $CH_4/H_2/Ar$ plasma. *(Etching conditions: 5 mTorr, 8% CH_4, $[H_2]/[Ar]$ = 1.5, 700 W, 95 sccm)*

Fig. 1 shows the plasma ions recorded in $CH_4/H_2/Ar$ plasma after the conditioning and cleaning processes. Above m/z 30, the main ions are Ar^+ (m/z 40) and ArH^+ (m/z 41). These

ions generate the Ar_2^+ ion at m/z 80. Although not shown, H_2^+ (m/z 2) and H_3^+ (m/z 3) are also detected. In low-pressure H_2/Ar discharges, it has been demonstrated that H_3^+ and ArH^+ ions are the dominant ions[38-40]. H_2^+ production primarily occurs through charge transfer from Ar^+ to H_2 (Eq 3a), while H_3^+ production involves proton transfer reactions (Eq 3b/c). Similarly, ArH+ production is mainly driven by proton transfer reactions (Eq 3d/e).

$$H_2 + Ar^+ \rightarrow H_2^+ + H \quad (3a)$$

$$H_2^+ + H_2 \rightarrow H_3^+ + H \quad (3b)$$

$$ArH^+ + H_2 \rightarrow Ar + H_3^+ \quad (3c)$$

$$H_2^+ + Ar \rightarrow H + ArH^+ \quad (3d)$$

$$Ar^+ + H_2 \rightarrow H + ArH^+ \quad (3e)$$

According to SRIM calculations (at E_{ions} = 200 eV), the sputtering yields of Ge, Sb, and Se with H_3^+ are approximately 0.02 atom/ion, while with ArH^+ ions, they are around 1 atom/ion. As a result, etching is predominantly influenced by Ar^+ and ArH^+ ion sputtering, suggesting that H_x^+ interactions with the etched elements (Ge, Sb, Se) primarily occur through gas-phase reactions.

In addition, two signals at m/z 89 and m/z 127 are associated to SF_3^+ and SF_5^+ residues related to other studies in SF_6 plasma[41]. The former overlaps with the $GeCH_x^+$ (m/z 82 to 93) and $SeCH_x^+$ (m/z 86 to 99) ion clusters. No fluorine-based etch product were found during mass spectrometry analysis.

1. *Hydride ions*

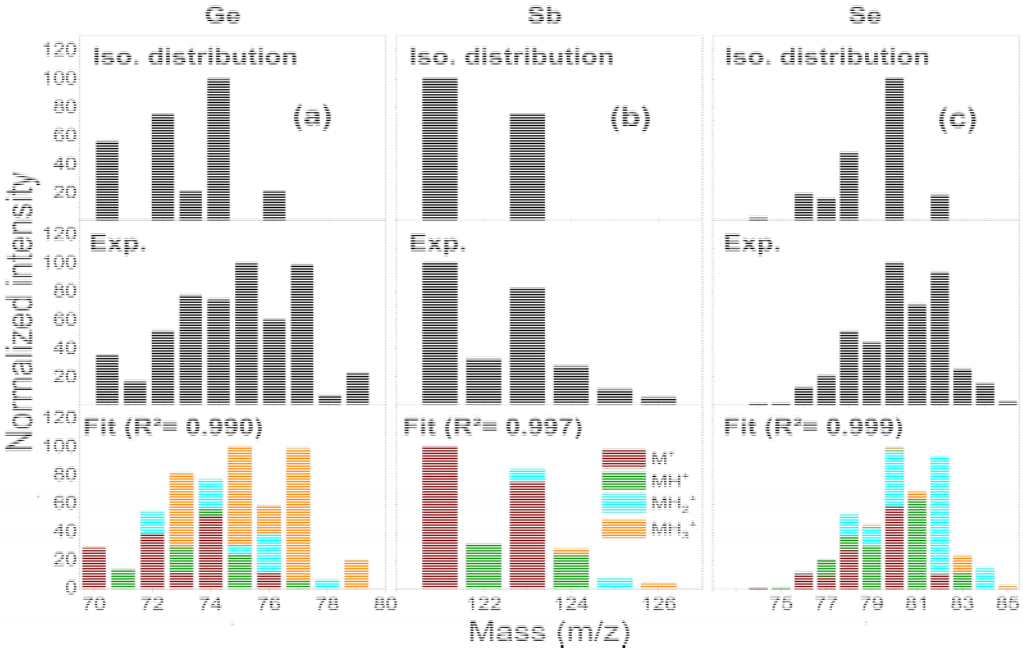

Figure 2: Natural isotopic distribution (top), Ion MS spectrum during H_2/Ar etching (middle) and predicted spectrum using the MLR analysis (bottom) of a) Ge/GeH_x^+ b) Sb/SbH_x^+ c) Se/SeH_x^+. *(Etching conditions: 6 mTorr, 700 W, [H_2]/[Ar] = 1, - 200 V, 130 sccm)*

Fig. 2 displays the natural isotopic distribution of Ge, Sb and Se; the recorded MS spectra during the etching of Ge, Sb and Se targets; and the modelling of GeH_x^+, SbH_x^+ and SeH_x^+ clusters. From m/z 70 to 85, the MS signals in the reference spectrum ($I \approx 10^3$ cps) remains two to three orders of magnitude lower than the signal recorded during the etching of Ge and Se ($I \approx 10^5/10^6$ cps). Therefore, the Ar_2^+ and $C_xH_y^+$ ions were not included in our calculation.

For the production of hydride ions, the obvious reactions are the proton transfer (Eq 4a/b), the direct ionization (Eq. 4*c*) and the dissociative ionization (Eq. 4*d*) by electronic impact of the stable molecules (*e.g.* GeH_4, SbH_3, SeH_2). However, the latter are not detected in a reactive neutral analysis, thus we expect that Eq 4c/d are not predominant. The presence of SeH_3^+ confirms that proton transfer reactions occur within the plasma.

$$Ar^+ + M \rightarrow Ar + M^+ \qquad (4a)$$

$$H_2^+ + M \rightarrow H + MH^+ \qquad (4b)$$

$$e^- + MH_y \rightarrow 2e^- + MH_y^+ \quad (4c)$$

$$e^- + MH_y \rightarrow 2e^- + MH_{y-1}^+ + H \quad (4d)$$

As can be seen in Fig. 2a, germanium has five stable isotopes from 70 to 76 amu whose two most abundant isotopes are ^{72}Ge (27.45%) and ^{74}Ge (36.52%). During the etching, the m/z 71, 75, 77 to 79 signals come from GeH_x^+ (x = 1-3) hydride ions. In the GeH_x^+ predicted spectrum, the addition of a GeH_4^+ pattern lacks of consistence, because if it were, $^{74}GeH_4^+$ would have contributed to the m/z 78 signal. Furthermore, $^{76}GeH_4^+$ (m/z 80) remains undetected or in negligible abundance in various studies concerning the GeH_4 fragmentation[42-44]. The coefficient of determination (R^2 = 0.990) indicates that the predicted spectrum fits the experimental data between m/z 70 and 79.

Antimony has two isotopes (^{121}Sb and ^{123}Sb) (Fig. 2b). The recorded SbH_x^+ cluster is delimited from m/z 121 ($^{121}Sb^+$) to 126 ($^{123}SbH_3^+$). The significant relative intensities of m/z 121 and 123 indicate that Sb^+ is the most abundant ion. Fragmentation of the stibine (SbH_3) has been examined in various cases, showing SbH^+ as the dominant ion among SbH_x^+, in which the ionization source was set with an electron energy above 25 eV[42,45]. However, in a low pressure H_2/Ar plasma, the mean kinetic electron energy is close to 2-3 eV, and only a fraction of the total electron density is above 8 eV[46,47]. During the etching process, it is unlikely to fully dissociate the SbH_3 into Sb^+, meaning that Sb atoms are likely ejected from the surface by Ar^+ sputtering, and subsequently charge transfer (Ar^+) or electron impact ionization produce the Sb^+ ion. Due to the weak signal of SbH_x^+ ions, it is believed that these species arise from proton transfer and the hydrogen recombination processes rather than SbH_3 dissociative ionization.

Selenium isotopic distribution exhibits a characteristic pattern, in which ^{80}Se is the most abundant isotope (Fig. 2c). The SeH_x^+ ion cluster is delimited from m/z 74 ($^{74}Se^+$) to 85 ($^{82}SeH_3^+$). As the weak signal at m/z 85 is solely due to the $^{82}SeH_3^+$ ion, it must be included into

the MRL analysis. An excellent match is found between the predicted SeH_x^+ spectrum and the experimental data ($R^2 = 0.999$). The former provides evidence of the important contributions of SeH^+ and SeH_2^+ ions.

GeH_x^+, SbH_x^+, SeH_x^+ clusters have GeH_3^+, Sb^+ and SeH_2^+ as dominant ions, respectively. Assuming that ionic species are produced by direct ionization of neutral species (GeH_4, SbH_3, SeH_2), the dominant species would have been GeH_2^+ [42,43], and SbH^+[42,45], and Se^+ or SeH_2^+ based on ionization threshold[48], respectively. However, the absence of $M_xH_y^+$ signal in radical analysis implies that other ionization mechanisms such as charge transfer (Ar^+), proton transfer (H^+), dissociation of $M_xH_y^+$ ions, must be taken into account. The formation of the dominant ions is a result of lower energy thresholds and/or higher cross sections of those reactions. However, the interpretation is limited due to the absence of data.

Negative ions are present in a H_2/Ar discharge, although not considered in this paper. The main reaction for H^- formation is dissociative attachment of H_2 molecules[49]. Hjartarson *et al.* demonstrated that H^- is among the dominant species in H_2/Ar discharges along with Ar^+ and ArH^+ ions[50]. Jiménez-Redondo *et al.* attributed the absence of H^- to the minimal contribution of highly vibrational states of H_2[47]. While the formation of $M_xC_yH_z^-$ species through electron attachment and vibrational excitation is possible, the main contributors of these negative ions are reactive neutral $M_xC_yH_z$ species, which are not detected by means of mass spectrometry.

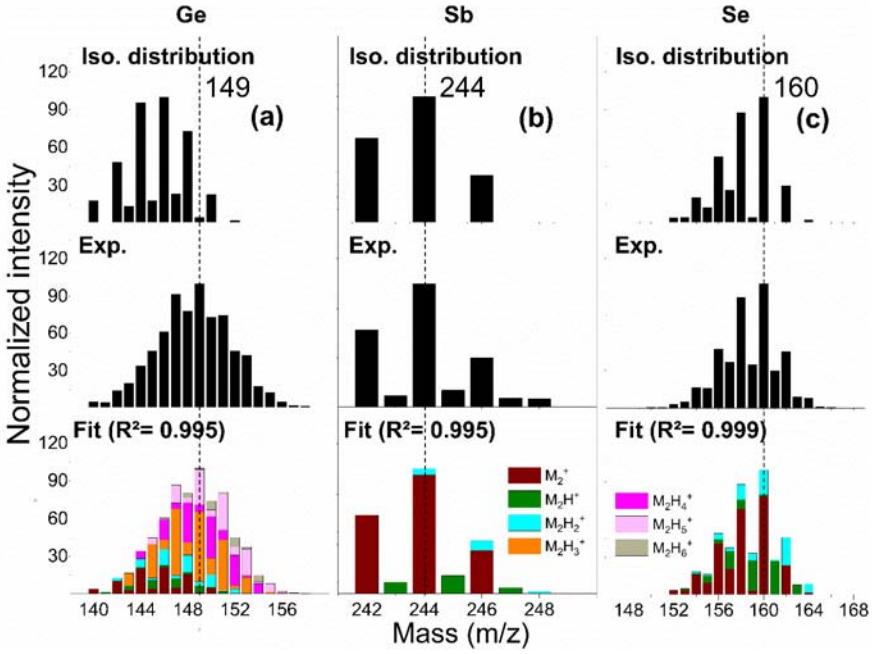

Figure 3: Natural isotopic distribution (top), Ion MS spectra during the H_2/Ar etching (middle) and predicted spectra using the MLR analysis (bottom) of a) $Ge_2/Ge_2H_x^+$ b) $Sb_2/Sb_2H_x^+$ c) $Se_2/Se_2H_x^+$. *(Etching conditions: 6 mTorr, 700 W, [H_2]/[Ar] = 1, - 200 V, 130 sccm)*

Ge_2 (Fig. 3a - top), Sb_2 (Fig. 3b - top) and Se_2 (Fig. 3c - top) theoretical abundance patterns are calculated using the isotopic distribution of Ge, Sb and Se atoms. One must consider etching as an atom by atom removal process. In other terms, M_2 molecules are not ejected from the surface. Consequently, the presence of $Ge_2H_x^+$ (Fig. 3a - middle), $Sb_2H_x^+$ (Fig. 3b - middle) and $Se_2H_x^+$ (Fig. 3c - middle) ions is a compelling evidence that ion-molecule reactions occur in the plasma. MLR analysis is performed on the latter experimental data to predict spectra based on the isotopic distribution of $Ge_2H_x^+$ (Fig. 3a - bottom), Sb_2H^+ (Fig. 3b - bottom) and Se_2H^+ (Fig. 3c - bottom). Analogously to the studies concerning the fragmentation of digermane (Ge_2H_6)[42,43], the $Ge_2H_x^+$ pattern is delimited from m/z 140 ($^{70}Ge_2^+$) to 158 ($^{76}Ge_2H_6^+$) (Fig. 3a). Thus, the MLR model contains all $Ge_2H_x^+$ (x = 6) ions. However, it has been showed that the desorption of digermane solely occurs at low temperature ($T_{substrate}$ < 200 K)[51]. Based on this consideration, the desorption of Ge_2H_6 is not conceivable in our etching

conditions ($T_{substrate}$ = 293 K). Thus, the production of $Ge_2H_x^+$ occurs mainly via hydrogen recombination and proton transfer in the plasma.

For the $Sb_2H_x^+$ cluster, the weak signal at m/z 248 suggests the presence of $Sb_2H_2^+$, which is added in the MLR model along with the $Sb_2H_x^+$ (x = 0, 1) isotopic distributions (Fig. 3b). The $Sb_2H_x^+$ cluster is formed via recombination between SbH_x species (both ionic and reactive neutral species), and a significant proportion of Sb^+ could explain the important contribution of the Sb_2^+.

The $Se_2H_x^+$ cluster is delimited from m/z 148 ($^{74}Se_2^+$) to 166 ($^{82}Se_2H_2^+$) (Fig. 3c). Inview of that information, the MLR is performed with three ions. Experimental data and the $Se_2H_x^+$ (x = 0-2) predicted spectrum share a similar feature with important signals of $^{80}Se_2^+$ (m/z 160), $^{78}Se_2^+$ (m/z 156) and $^{78}Se^{80}Se^+$ (m/z 158) predominately due to the Se_2^+ ions. Other $Se_2H_x^+$ contributions are found at m/z 161, 163, 165 and 166.

2. *Organometallic ions*

There are valid reasons why methane-based plasmas are not commonly used for Ge (or Si) etching. Firstly, the adsorption of hydrogen on germanium is influenced by the gas temperature, with hydrogen desorption from GeH_4 observed at lower temperatures (< 300K)[52]. Additionally, thermal dissociation of germanium hydride products can occur at higher gas temperatures (T_{gas} > 300)[53]. Consequently, significantly increasing the energy of bombarding ions becomes necessary to etch the C_xH_y and Ge-$(C)_x$ species. In our study, the applied bias potential is sufficiently high to prevent CH_x deposition on the material.

It is worth noting that the electron impact cross-sections of CH_4 into CH_2^+ and CH_4 into CH_2 are lower compared to CH_4 into CH_3^+ in the energy range of 10-50 eV[54,55]. Therefore, we consider CH_3^+ to be the dominant ion among the CH_x^+ ions. Furthermore, considering the sputtering yields for Ge, Sb, and Se with CH_3^+ (at -150V) is approximately 0.35, whereas with Ar+ it is around 0.6 atom/ion. Based

on this information, it is likely that CH_3^+ contributes to the physical etching process.

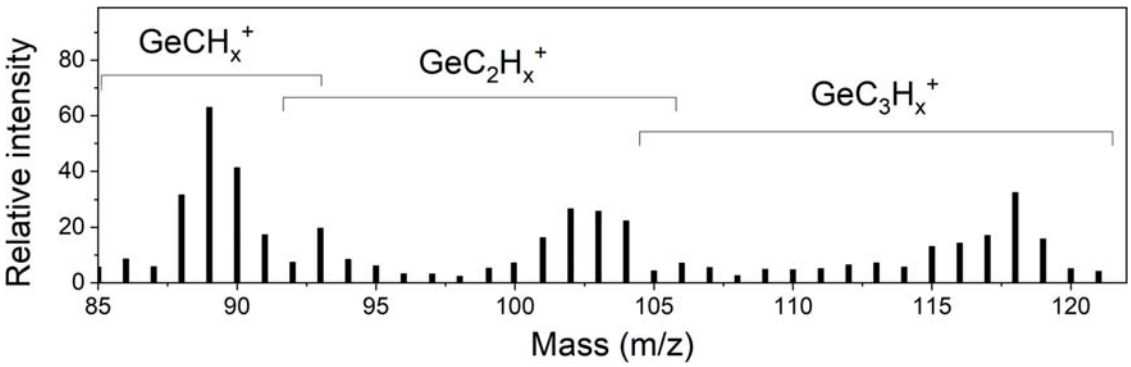

Figure 4: Ion mass spectrum recorded during $CH_4/H_2/Ar$ etching of Ge. *(Etching conditions: 5 mTorr, 8% CH_4, [H_2]/[Ar] = 1.5, 700 W, -150V, 95 sccm)*

As displayed in Fig. 4, organogermanium ion clusters are detected from m/z 85 to 121, with maxima at m/z 89, 103 and 118. Considering that $^{74}Ge(CH_3)H_3^+$ is located at m/z 92, the m/z 93 signal is not associated to the $GeCH_x^+$ ion cluster. Furthermore, the decomposition is not performed due to weak signals of the $GeC_xH_y^+$ clusters as well as an overlapping between other products (SeC_xH_y residues, $C_xH_y^+$ and SF_3^+). Studies concerning the fragmentation of tetramethylgermane ($Ge(CH_3)_4$; TeMeGe) also exhibit three ion clusters[56,57]: $GeCH_x^+$, $GeC_2H_x^+$and $GeC_3H_x^+$. Above m/z 121, $GeC_4H_x^+$ ion cluster remains undetected. The latter has been reported during the fragmentation of the diethylmonogermane and diethyldigermane[58]. Furthermore, the desorption of TeMeGe has been reported optimal at $T_{substrate}$ = 140 K[59]. Above that substrate temperature, Greenlief *et al.* suggest that TeMeGe is decomposed. In the current substrate temperature, the desorption of TeMeGe is hardly conceivable.

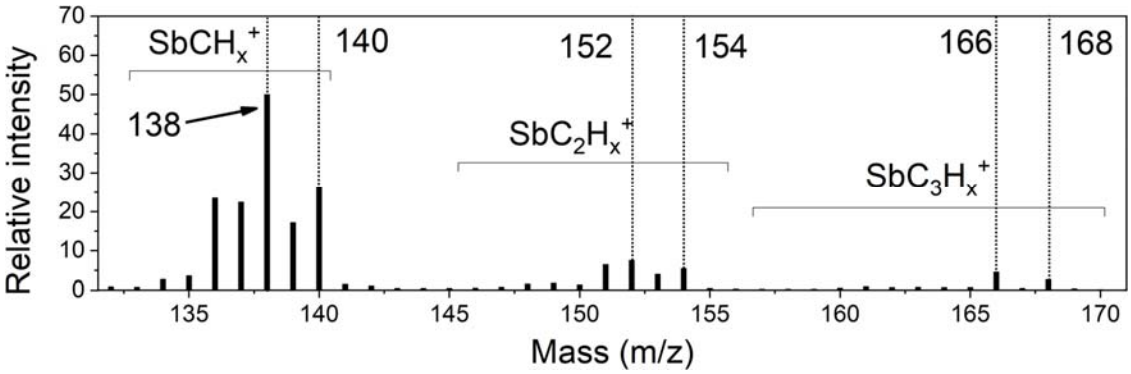

Figure 5: Ion mass spectrum recorded during $CH_4/H_2/Ar$ etching of Sb. (Etching conditions: 5 mTorr, 8% CH_4, [H_2]/[Ar]=1.5, 700 W, -150V, 95 sccm)

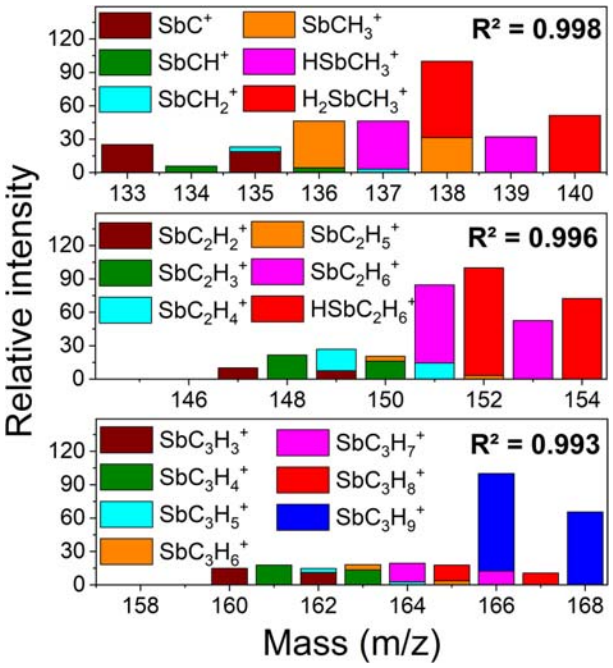

Figure 6: Predicted $SbC_xH_y^+$ spectra using the MLR analysis on MS data displayed in Fig. 5.

MS spectrum recorded during the etching of the Sb ingot is presented in Fig. 5. As bio-organometallic compounds, methylantimony (i.e. methylstibine; MeSb), dimethylantimony (DMeSb) and trimethylantimony (TMeSb) molecules are usually extracted from water or biological samples as moss, snails and fungi[60-63], in which three separate ion clusters are distinguished: $SbCH_x^+$, $SbC_2H_x^+$ and $SbC_3H_x^+$. The signals at m/z 140, 154 and 168 are exclusively associated to the $H_2{}^{123}SbCH_3^+$, $H^{123}Sb(CH_3)_2^+$ and $^{123}Sb(CH_3)_3^+$ ions, respectively. In that respect, the MLR of the three clusters should take into account all $SbCH_x^+$ (x = 0-5), $SbC_2H_x^+$ (x = 0-7) and $SbC_3H_x^+$ (x = 0-9) ions (Fig. 6). Nevertheless, $SbC_2H_x^+$ (x = 0-1) and $SbC_3H_x^+$ (x = 0-2) were not plotted due to their negligible relative intensities. Interestingly, the $HSbC_2H_6^+$ is not systematically detected in studies concerning the fragmentation of TMeSb, even when some experiments rely on a similar ionization source[61,64]. It demonstrates that the disparities come from the parameters of the ionization source. For the SbC_3H^+ ion cluster, studies regarding the fragmentation of trimethylantimony[60,64,65] and our experiment show clearly $SbC_3H_9^+$ (m/z 166 and 168) as the dominant ion among the $SbC_3H_x^+$ cluster, although the spectra differ. In our experiment, unique features are observed due to the $SbC_3H_x^+$ (x = 3-8) contributions in the range

of m/z 160 to 167. It is not clear if the main ions ($H_2SbCH_3^+$, $HSbC_2H_6^+$ and $SbC_3H_9^+$) originate from the dissociative ionization at low electron energy, of the MeSb, DMeSb and TMeSb molecules or from the recombination between Sb and CH_x reactive neutral species.

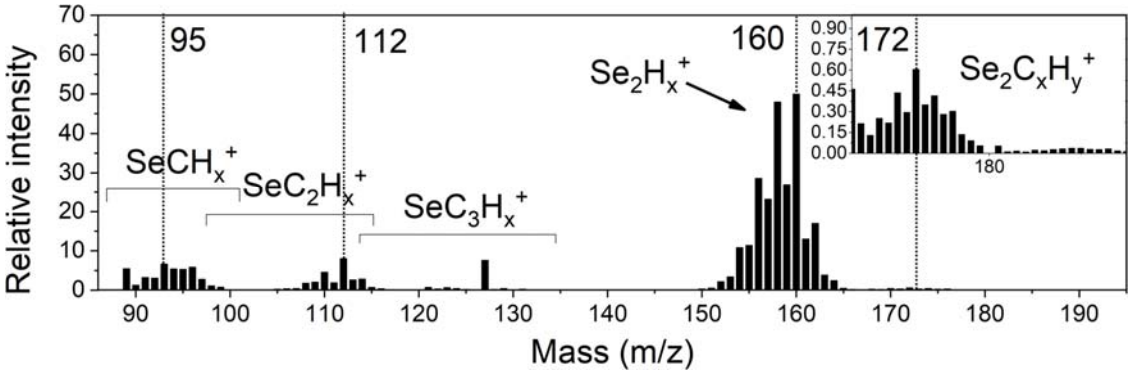

Figure 7: Ion mass spectrum recorded during CH_4/H_2/Ar etching of Se. *(Etching conditions: 5 mTorr, 8% CH_4, $[H_2]/[Ar]$=1.5, 700 W*, - 150V, 95 sccm)

Biological selenium compounds are formed by successive recombination between CH_x reactive neutral species and Se. The biochemical reaction refers to the methylation process which enables the formation of stable species as methylselane (CH_3-SeH; MeSe) and dimethylselenium (CH_3-Se-CH_3; DMeSe)[66,67]. By comparison with the fragmentation of these two stable molecules[68,69], two organoselenium ion clusters are identified as $SeCH_x^+$ and $SeC_2H_x^+$ (Fig. 7). The weak signals between m/z 115 and 125 suggest the formation of $SeC_3H_x^+$ ions, but no $SeC_4H_x^+$ cluster is detected as it is evidenced during the fragmentation of the diethylselenide (DEtSe)[69]. We conclude that the latter is not produced during the etching process. The signals at m/z 89 and m/z 127 are the SF_3^+ and SF_5^+ features presented in the reference spectrum (Fig. 1). The $SeC_2H_x^+$ cluster is delimited from m/z 98 to 115 and implies the existence of the $H_3Se(CH_3)_2^+$ ion, but the bonding between hydrogen and selenium is not clear. In addition, the decomposition is not reliable due to the high number of ions and the overlapping with the $SeC_3H_x^+$cluster. MLR analysis is applied for the $SeCH_x^+$ and $Se_2CH_x^+$ ion clusters (Fig. 8). Above m/z 150, the fragmentation of the dimethyldiselenide (CH_3-Se-Se-CH_3; DMeDSe) has been investigated[68,70], and as in our spectra, these studies contain the $Se_2C_xH_x^+$ ion clusters. Based on the MLR analysis, $Se_2H_x^+$ (see Fig. 3) and $Se_2CH_x^+$ clusters present similar patterns with maxima at m/z 160 and 172 due to the Se_2^+ and Se_2C^+ ions, respectively.

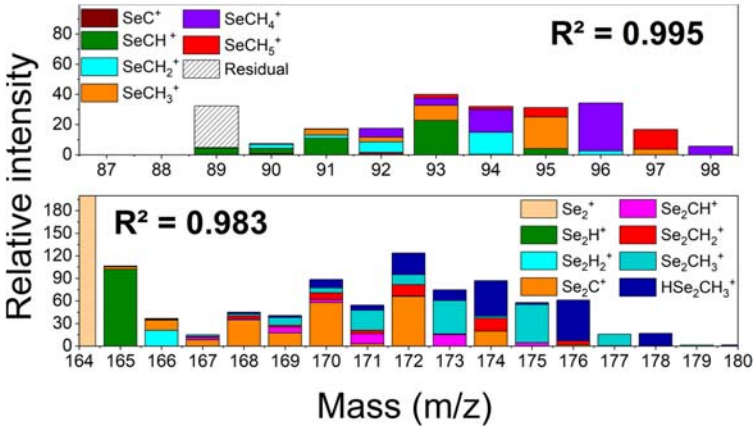

Figure 8: Predicted $SeCH_x^+$ and $Se_2CH_x^+$ spectra using the MLR analysis on MS data displayed in Fig. 7.

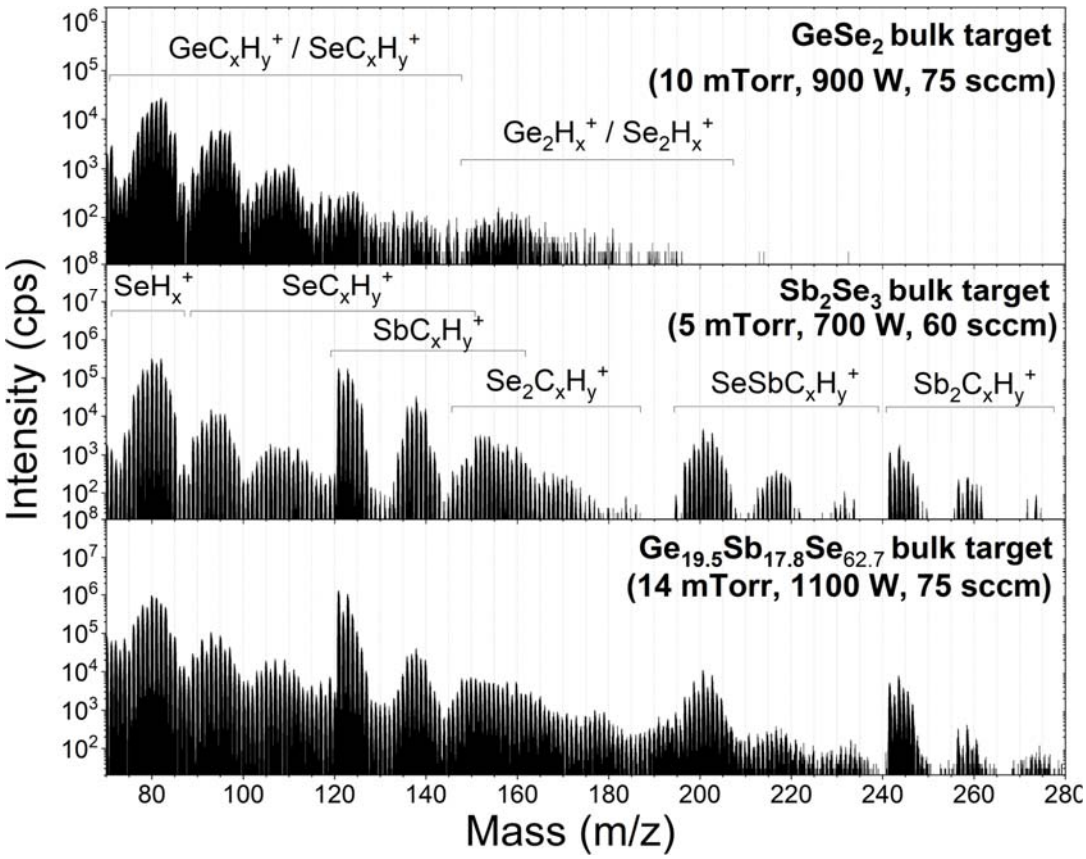

Figure 9: Ion mass spectra recorded during the etching of $GeSe_2$ glass target, Sb_2Se_3 bulk target and $Ge_{19.5}Sb_{17.8}Se_{62.7}$ glass target. *(Etching conditions: 8% CH_4, $[H_2]/[Ar]$=1.5, - 150 V)*

As shown in Fig. 9, the methane-based etching of the $GeSe_2$ glass target, the Sb_2Se_3 bulk target and the $Ge_{19.5}Sb_{17.8}Se_{62.7}$ glass target generates a considerable number of products. For $GeSe_2$, no feature other than the previously identified $Ge_xC_yH_z^+$ and $Se_xH_y^+$ are detected. Interestingly, in the case of the

Sb_2Se_3 and $Ge_{19.5}Sb_{17.8}Se_{62.7}$ MS spectra, we observe a large cluster between m/z 195 to 222 that fits well with a $SeSbC_xH_y^+$ cluster, which is a strong indication that ion-molecule reactions occur between different etching products. During the etching of the Ge-Sb-Se target, another cluster is present between m/z 190 to 196, which could be related to the mixed $GeSbH_x^+$ ion cluster, but in this particular case, the large number of ion clusters makes the MLR analysis not reliable. In addition, with optimized plasma conditions, weak signals of the $Sb_2C_xH_y^+$ ions clusters are detected from m/z 255 to 275.

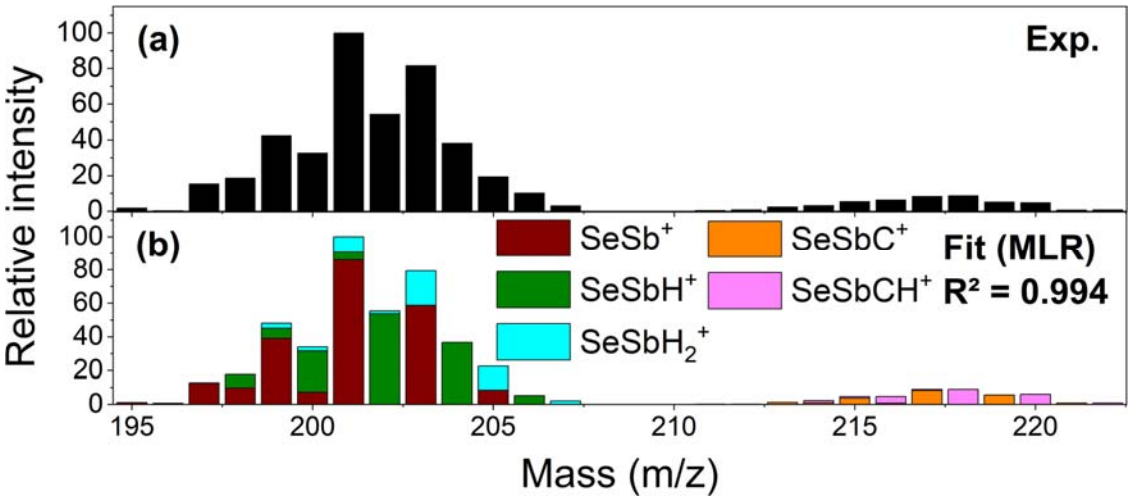

Figure 10: (a) MS data recorded during the etching of the Sb_2Se_3 bulk target (b) The related predicted spectrum (Fit).

As displayed in Fig. 10, the MLR analysis is performed between m/z 195 to 222, including $SeSbH_x^+$ and $SeSbCH_x^+$ isotopic distributions in the model. The addition of the $SeSbH^+$ to the $SeSb^+$ theoretical pattern is justified by the important signal at m/z 202. Then, the $SeSbH_2^+$ pattern is also added because of the m/z 207 signal ($^{82}Se^{123}SbH_2^+$). For the $SeSbCH_x^+$ cluster, no signal above m/z 222 is detected. Because of that, $SeSbCH_2^+$ is not included in the MLR calculation. As interpreted with the predicted spectrum, $SeSb^+$ and $SeSbCH^+$ are the dominant ions among their respective cluster. The formation of these clusters is coherent since M_2H^+ (M = Ge, Sb, Se) are mostly generated from the same reactions.

It is important to note that the ion signals observed are directly influenced by various factors, including the incoming flux of etched elements (*i.e.,* the etch rate), the concentrations of H, H^+, CH_x, ,

CH_x^+ and Ar/ArH^+ species in the plasma, the electronic temperature, the electronic density, the density of stable etch products (if formed), and the gas temperature, which affects recombination processes. A methane-based plasma chemistry can be employed for etching the Ge-Se, Sb-Se, and Ge-Sb-Se systems. Additionally, it should be emphasized that the presence of a C_xH_y polymer covering the surface is not necessarily an outcome.

3.2. In situ XPS analysis

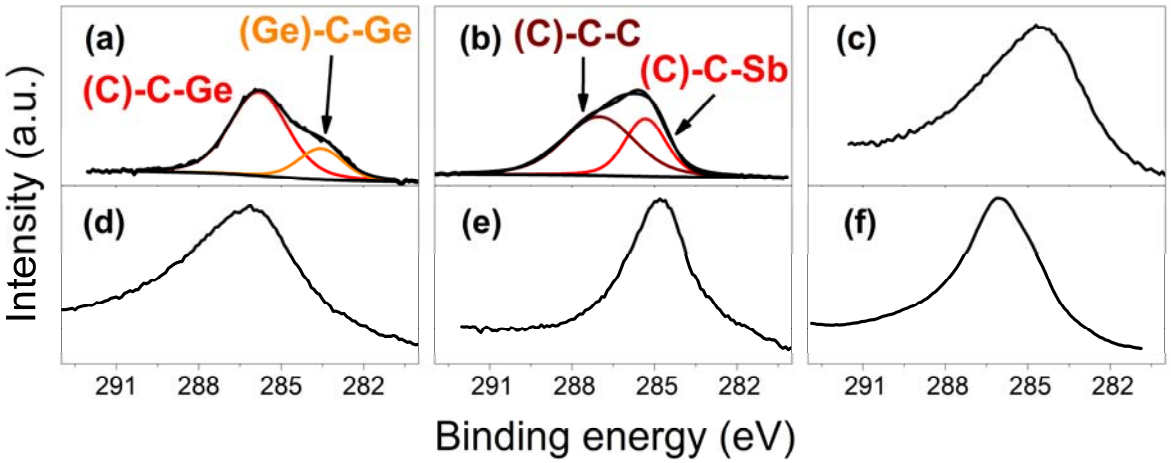

Figure 11: C 1s XPS spectra of etched (a) Ge (b) Sb (c) Se (d) $Ge_{39}Se_{61}$ thin film (e) Sb_2Se_3 (f) $Ge_{19}Sb_{21}Se_{60}$. *(Etching conditions: $CH_4/H_2/Ar$ plasma, 3 mTorr, 4% CH_4, $[H_2]/[Ar]$=1.5, 700 W, - 150 V and 75 sccm)*

Fig. 11 presents the Se, Ge, Sb, $Ge_{39}Se_{61}$, Sb_2Se_3, $Ge_{19}Sb_{21}Se_{60}$ XPS spectra after etching in $CH_4/H_2/Ar$ plasma. On the Ge surface (Fig. 11a), there is evidence of Ge-C bonding at 283.5 eV, which is consistent with the values reported in literature[71,72]. The interpretation of the Sb spectrum in Fig. 11b is not as straightforward. As Sb and C are the two elements at the surface of the material, the (C)-C-Sb environment (BE = 285.3 eV) is expected at lower value of binding energy, and the contribution at 286.9 eV is assigned to the C-C bonding. These organometallic contributions come from the adsorption of CH_x radicals or redeposit of $M_xC_yH_z$ (M = Ge, Sb) species. The decomposition of the Se (Fig. 11c) $Ge_{39}Se_{61}$ (Fig. 11d), Sb_2Se_3 (Fig.

11e), $Ge_{19}Sb_{21}Se_{60}$ (Fig. 11f) C 1s XPS spectra should take into account the Se $L_3M_3M_{4,5}$[73] as well as the C-Ge(Se) and C-Sb(Se) environments, and similarly to the Se XPS spectrum, these spectra cannot be decomposed. Besides, the kinetic energy of Se $L_3M_3M_{4,5}$ is affected by the environment of Se[74,75], which is obviously modified by the etching process.

Table 1, Table 2 and Table 3 list the fit values used for the decomposition of the core levels such as the Binding Energy (BE), the Full Width at Half Maximum (FWHM), the spin-orbit splitting (ΔE) and the relative area of different peaks or doublets within the same core level. Following the etching process, it is important to note that the environment of Ge and Sb atoms within the surface layer (0 to 1 nm) can differ significantly from that of the near-surface region (1 to 100 nm). That is why it is of interest to note the change of relative area of each component between two spectral regions well separated in energy (*i.e.* Ge $2p_{3/2}$ and Ge 3d; Sb 3d and Sb 4d). For a given binding energy, 95% of the photoelectron intensity corresponds to a depth of analysis which equates to three times the inelastic mean free path (3λ). The latter is calculated from a predictive formula thanks to the software provided by NIST[76]. IMFP calculations require the band gaps[77,78], the compounds specific weight and the number of valence electrons per atom.

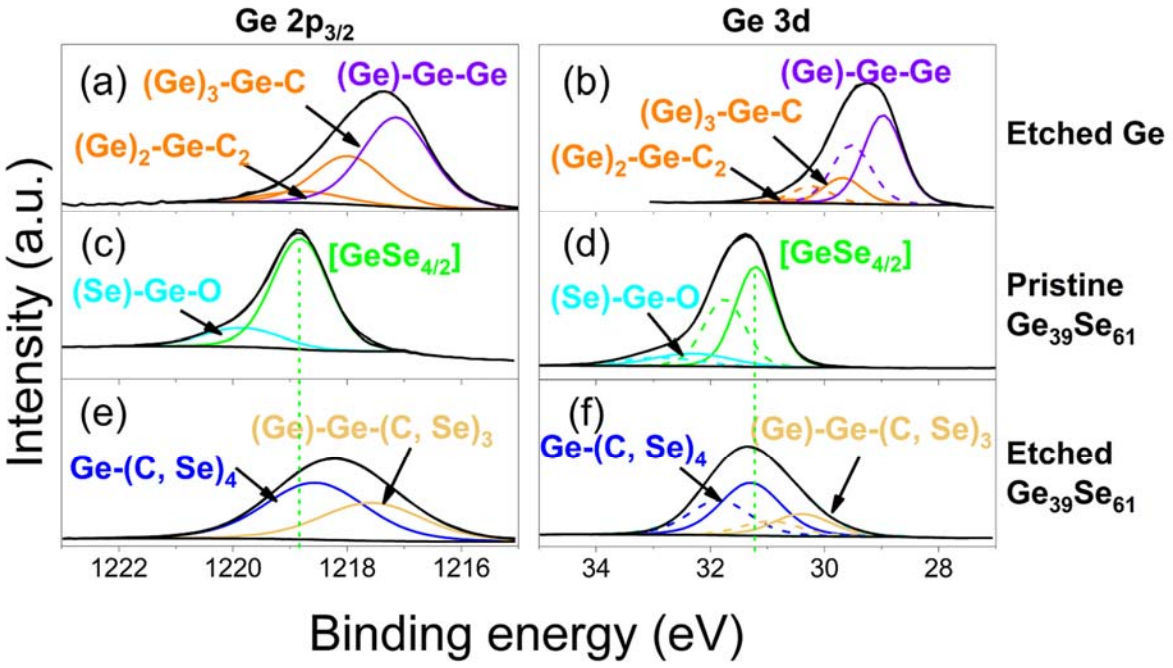

Figure 12: XPS spectra of etched Ge (a) Ge $2p_{3/2}$ (b) Ge 3d; pristine $Ge_{39}Se_{61}$ thin film (c) Ge $2p_{3/2}$ (d) Ge 3d; etched $Ge_{39}Se_{61}$ thin film (e) Ge $2p_{3/2}$ (f) Ge 3d. *(Etching conditions: $CH_4/H_2/Ar$ plasma, 3 mTorr, 4% CH_4, $[H_2]/[Ar]$=1.5, 700 W, - 150 V and 75 sccm)*

Fig. 12 presents the decomposed Ge $2p_{3/2}$ and Ge 3d core levels of Ge and $Ge_{39}Se_{61}$ samples. The homopolar (Ge)-Ge-Ge contributions are located 1217.2 eV (Ge $2p_{3/2}$) and 29.0 eV (Ge 3d). The (Ge)-Ge-C_x (x = 1-2) species originate from the adsorption of the CH_x reactive neutrals or a GeC_xH_y redeposit. As demonstrated by few studies about $Ge_{1-x}C_x$ thin films, the examined Ge 3d core level is centered between 29.5 to 30.2 eV according to the deposition conditions[71,79,80]. To that extend, it is expected that our (Ge)-Ge-C_x contributions are specific to the etching conditions and the initial composition of the investigated thin film.

At the surface of the pristine $Ge_{39}Se_{61}$ thin film (Fig. 12c/d), the dominant contribution is assigned to the [$GeSe_{4/2}$] motif. Our binding energy value (BE = 31.3 eV) is consistent with literature regarding the Ge-Se system, in which the Ge-Se contribution ranges from 30.5 to 31.5 eV[31-34,81]. Note that the surface is oxidized due to air exposure prior to XPS analysis, resulting in a small contribution of (Se)-Ge-O chemical state. Turning to the etched $Ge_{39}Se_{61}$ thin film, the

contributions in Ge $2p_{3/2}$ (Fig. 12e) and Ge 3d (Fig. 12f) are believed to originate from the (Ge)-Ge-(Se, C)$_3$ entities. It is somewhat problematic to distinguish the [$GeSe_{4/2}$] motif from the carbide $(Se)_{4-x}$-Ge-$(C)_x$ since carbon and selenium have the same electronegativity (2.55). In practice, the binding energy values of Ge-$(C)_x$ and Ge-$(Se)_x$ (x = 1-4) are virtually identical. However, neighboring methyl groups may affect slightly the electron density of the electron shells of Ge atoms.

		Ge $2p_{3/2}$				Ge $3d_{5/2}$ (ΔE = 0.55 eV)			
		BE (eV)	FWHM (eV)	3λ (nm)	Rel. area	BE (eV)	FWHM (eV)	3λ (nm)	Rel. area
Etched Ge	(Ge)-Ge-Ge	1217.2	1.42	2.6	100	29	0.82	8.5	100
	$(Ge)_3$-Ge-C	1218.0	1.45		54.8	29.7	0.80		28.0
	$(Ge)_2$-Ge-C_2	1218.8	1.70		15.1	30.6	0.93		4.4
Pristine $Ge_{39}Se_{61}$	[$GeSe_{4/2}$]	1218.8	1.10	2.5	100	31.3	1.11	8.4	100
	(Se)-Ge-O	1219.5	1.81		32.5	32.5	1.33		19.2
Etched $Ge_{39}Se_{61}$	(Ge)-Ge-(C, Se)$_3$	1217.9	2.34		97.0	30.7	1.31		59.2
	$(Se)_{4-x}$-Ge-C_x	1218.8	2.11		100	31.5	1.17		100

Table 1: Fit values extracted from Ge $2p_{3/2}$ and Ge 3d XPS spectra (Fig. 12). *BE: Binding Energy (± 0.2 eV); FWHM: Full Width at Half Maximum (± 0.05 eV); ΔE: spin-orbit splitting (± 0.05 eV).*

From the comparison between the fit values of Ge $2p_{3/2}$ ($3\lambda \approx 2.5$ nm) and Ge 3d ($3\lambda \approx 8.5$ nm) (Table 1), the drop of the (Ge)-Ge-C_x and (Ge)-Ge-(C, Se)$_3$ relative areas is interpreted as a carbon depletion along the depth of analysis. Thus, those environments are mostly found in the first surface layers (0 to 1 nm).

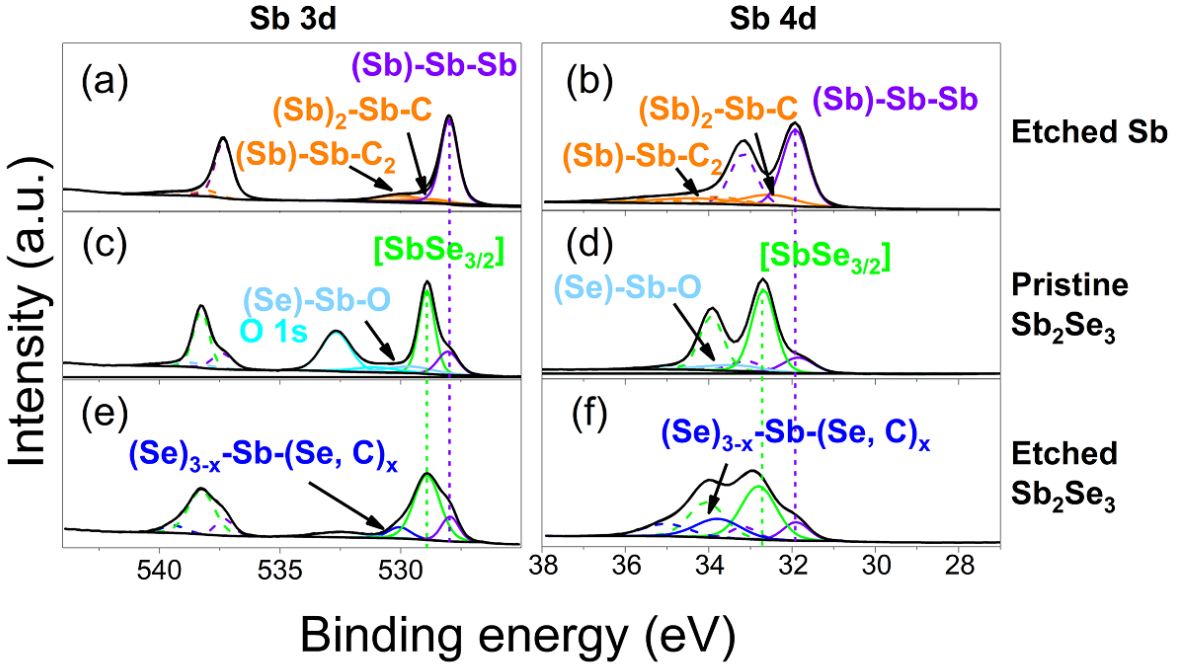

Figure 13: XPS spectra of etched Sb (a) Sb 3d (b) Sb 4d; pristine Sb_2Se_3 (c) Sb 3d (d) Sb 4d; etched Sb_2Se_3 (e) Sb 3d (f) Sb 4d. *(Etching conditions: $CH_4/H_2/Ar$ plasma, 3 mTorr, 4% CH_4, $[H_2]/[Ar]$=1.5, 700 W, - 150 V and 75 sccm)*

As displayed in Fig. 13, the energy regions of 545 - 525 eV and 38 - 31 eV correspond to the Sb 3d and Sb 4d core levels, respectively. The homopolar Sb-Sb bond is positioned at 528.0/528.1 eV (Sb $3d_{5/2}$) and 31.9/32.0 eV (Sb $4d_{5/2}$). Based on the energy shifts on the Sb XPS spectra (Fig. 13a/b), the doublets at higher values of binding energy originate from the (Sb)-Sb-C_x (x = 1, 2) entities. In the case of the pristine Sb_2Se_3 XPS spectra (Fig. 13c/d), there is initially a (Sb)-Sb-Sb environment and the dominant contribution is the [$SbSe_{3/2}$] motif. **Regarding the pristine Sb_2Se_3 XPS spectra (Fig. 13c/d), the initial environment is characterized by (Sb)-Sb-Sb bonds, with the dominant contribution from the [$SbSe_{3/2}$] motif. The presence of the (Se)-Sb-O environment in the pristine sample is a result of air exposure prior to the XPS analysis. It is important to note that the Sb_2Se_3 XPS analysis was conducted on Sb_2Se_3 powder obtained by grinding the bulk target. The presence of oxygen in Fig. 13e can be attributed to trapped oxygen during the grinding process.**

After the etching process (Fig. 13e/f), Sb atoms exhibit several environments starting from the (Sb)-Sb-Sb and [$SbSe_{3/2}$] motif, which remain the dominant contributions. However, the bonding between carbon and antimony atoms eventually generates the (Sb)-Sb-C_x (see Fig. 13a/b) and the (Se)-Sb- C_x environments. The attribution of a specific environment for the doublet at 529.0/32.9 eV and 529.8/33.8 eV cannot be done for the etched sample. Their larger FWHMs are interpreted as an overlapping between the [$SbSe_{3/2}$] motif, (Sb)-Sb-C_x and (Se)-Sb-C_x environments. Thus, these doublets are denominated $(Se)_{3-x}$-Sb-$(Se, C)_x$.

Turning to the Sb sample, between Sb 3d (3λ = 6.5 nm) and Sb 4d (3λ = 8.5 nm), it seems that the relative abundance of the (Sb)-Sb-$(C)_x$ environments increases with the depth of analysis (Table 2). Such result is rather counterintuitive assuming that most of the CH_x reactive neutrals are adsorbed on the surface. In the Sb 4d core level spectrum of the Sb_2Se_3 powder, the spin-orbit splitting (ΔE = 1.25 eV) entangles the interpretation because of the overlapping between all Sb $4d_{5/2}$ and Sb $4d_{3/2}$ contributions (Sb-Sb, Sb-Se and Sb-C).

		Sb $3d_{5/2}$ (ΔE = 9.35 eV)				Sb $4d_{5/2}$ (ΔE = 1.25 eV)			
		BE (eV)	FWHM (eV)	3λ (nm)	Rel. area	BE (eV)	FWHM (eV)	3λ (nm)	Rel. area
Etched Sb	(Sb)-Sb-Sb	528.0	0.84	6.5	100	31.9	0.73	8.5	100
	$(Sb)_2$-Sb-C	528.7	1.08		12.5	32.5	1.00		15.6
	(Sb)-Sb-C_2	530.0	2.33		17.9	33.2	2.37		23.0
Pristine Sb_2Se_3	(Sb)-Sb-Sb	528.1	1.01	5.4	36.2	31.9	0.86	7.5	24.3
	[$SbSe_{3/2}$]	529.0	0.78		100	32.8	0.67		100
	(Se)-Sb-O	529.4	2.37		23.7	33.8	1.70		17.7
Etched Sb_2Se_3	(Sb)-Sb-Sb	528.1	0.86		26.0	32.0	0.74		25.4
	[$SbSe_{3/2}$]	529.0	1.27		100	32.9	1.00		100
	$(Se)_{3-x}$-Sb-$(C, Se)_x$	529.8	1.11		15.3	33.8	1.28		45.3

Table 2: Fit values extracted from Sb 3d and Sb 4d XPS spectra (Fig. 13). *BE: Binding Energy (± 0.2 eV); FWHM: Full Width at Half Maximum (± 0.05 eV); ΔE: spin-orbit splitting (± 0.05 eV).*

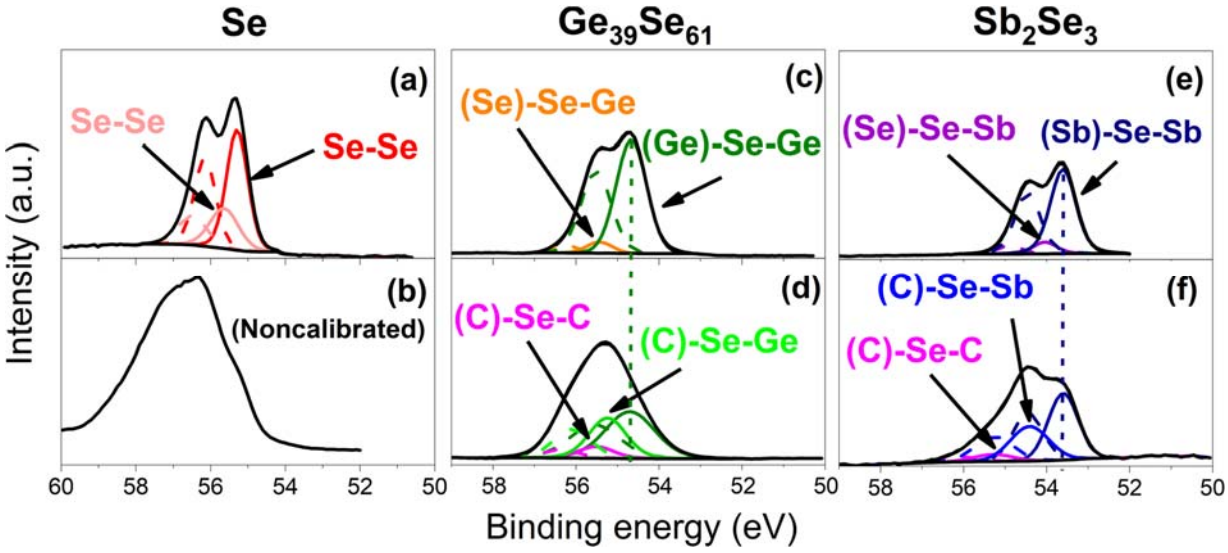

Figure 14: Se 3d XPS spectra of Se (a) pristine (b) etched; $Ge_{39}Se_{61}$ thin film (c) pristine (d) etched; Sb_2Se_3 powder (e) pristine (f) etched. *(Etching conditions: $CH_4/H_2/Ar$ plasma, 3 mTorr, 4% CH_4, $[H_2]/[Ar]$=1.5, 700 W, - 150 V and 75 sccm)*

Fig. 14 illustrates the fitting of Se 3d of Se, $Ge_{39}Se_{61}$ and Sb_2Se_3 XPS spectra before and after the $CH_4/H_2/Ar$ etching process. On the pristine selenium sample (Fig. 14a), a first Se-Se doublet is located at 55.3 eV. Nevertheless, the spectra cannot be fitted with solely one doublet once the spin-orbit splitting (0.85 eV) is fixed. Thus, a second doublet is needed (BE = 55.7 eV), which is likely describing another structure within the material. This is consistent with the fact that vitreous selenium is composed of selenium-rings and selenium-chains[82,83]. As displayed in Fig. 14b, the Se etched sample is not decomposed. Its decomposition would have required at least four doublets which overlap because of the low spin-orbit splitting (ΔE = 0.85 eV). As such, the decomposition lacks of physical explanations. But assuming that (Se)-Se-Se and (C)- Se-C environments are similar in term of binding energy, we presume the broadening as a consequence of H and CH_x reactive neutral bonding. Besides, the energy calibration is not performed because the C-H bond cannot be distinguished from the Se $L_3M_{2,3}M_{4,5}$ Auger in C 1s core level spectrum (Fig. 11).

$Ge_{39}Se_{61}$ and Sb_2Se_3 pristine Se 3d core level spectra are decomposed with two doublets (Fig. 14c/e). It is assumed that the doublets, positioned at 54.7 eV and 53.6 eV, correspond to the (Ge)-Se-Ge (*i.e.* [$GeSe_{4/2}$]) and (Sb)-Se-Sb (*i.e.* [$SbSe_{3/2}$]), respectively. The second doublets are allocated to (Se)-Se-Ge and (Se)-Se-Sb environments due to the shift to higher binding energy as pointed out in Table 3.

The environment of Se atoms differs from those of Ge and Sb atoms. Indeed, after the etching process, Se atoms are twofold coordinated with Ge, Sb and C. As can be seen in Fig. 14d/f, the (C)-Se-C entity also broaden the $Ge_{39}Se_{61}$ and Sb_2Se_3 XPS spectra to higher values of binding energy.

		Pristine (ΔE = 0.85 eV)				Etched (ΔE = 0.85 eV)		
		3λ (nm)	BE (eV)	FWHM (eV)	Rel. Area	BE (eV)	FWHM (eV)	Rel. Area
Se-Se	Se-Se	8.46	55.3	0.67	100			
	Se-Se		55.6	0.91	46.5			
$Ge_{39}Se_{61}$	(Ge)-Se-Ge	8.40	54.7	0.86	100	54.7	1.40	100
	(Se)-Se-Ge		55.4	0.76	10.9			
	(C)-Se-Ge					55.2	1.00	63.9
	(C)-Se-C					55.6	0.95	21.8
Sb_2Se_3	(Sb)-Se-Sb	7.41	53.6	0.72	100	53.5	0.85	100
	(Se)-Se-Sb		54.0	0.66	7.8			
	(C)-Se-Sb					54.4	1.09	66.7
	(C)-Se-C					55.3	1.11	13.7

Table 3: Fit values extracted from Se 3d XPS spectra (Fig. 14). *BE: Binding Energy (± 0.2 eV); FWHM: Full Width at Half Maximum (± 0.05 eV); ΔE: spin-orbit splitting (± 0.05 eV).*

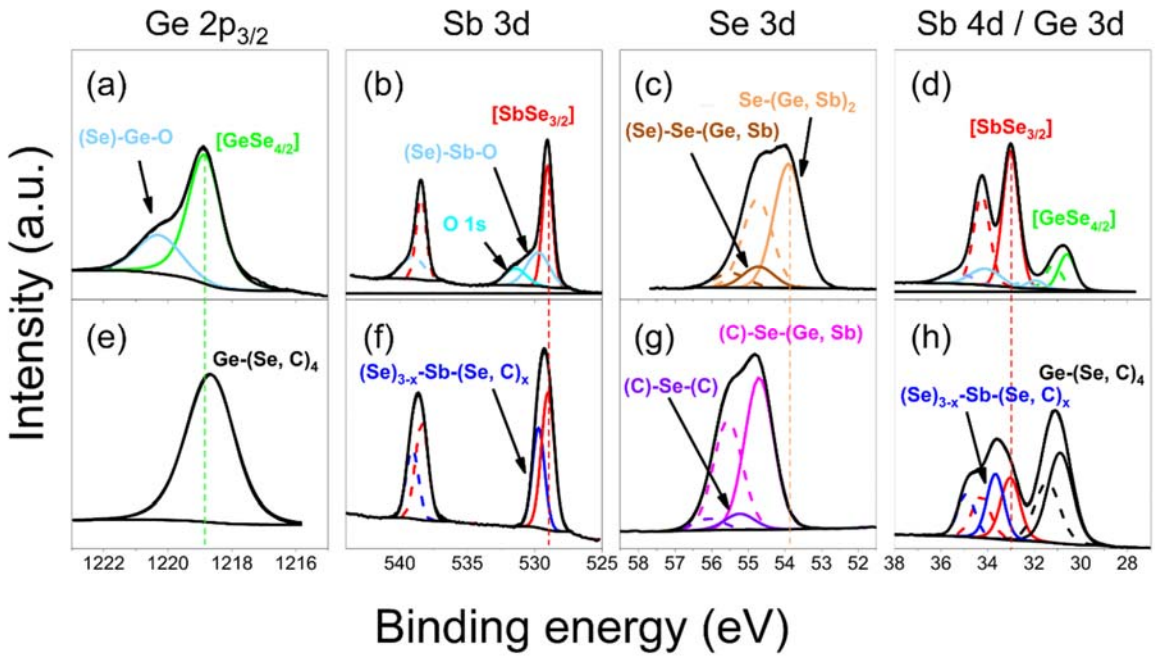

Figure 15: XPS spectra after the etching of $Ge_{19}Sb_{21}Se_{60}$ thin film of Ge $2p_{3/2}$ (a) pristine (b) etched; Sb 3d (c) pristine (d) etched; Se 3d (e) pristine (f) etched; Sb 4d / Ge 3d (g) pristine (h) etched *(Etching conditions: $CH_4/H_2/Ar$ plasma, 3 mTorr, 4% CH_4, $[H_2]/[Ar]$=1.5, 700 W, - 150 V and 75 sccm)*

Fig. 15 shows the XPS spectra before and after the etching of the $Ge_{19}Sb_{21}Se_{60}$ thin film. It is admitted that the $[GeSe_{4/2}]$ and $[SbSe_{3/2}]$ motifs are identified as the most dominant units in the stoichiometric Ge-Sb-Se system[28,84-86].

On the Ge $2p_{3/2}$ core level, the overlapping between carbides and selenides is evidenced with similar binding energies of the $[GeSe_{4/2}]$ motif (Fig. 15a) and (Se)-Ge-(C, Se)$_x$ species (Fig. 15b). The latter envelops more than one chemical state assuming that (Se)$_x$-Ge-C_{4-x} environments are formed at the surface. We note the absence of the (Ge)-Ge-(C, Se)$_x$ as observed for the etched $Ge_{31}Se_{69}$ thin film.

Turning on the Sb 3d core level, the etching generates the nondistinct (Se)-Sb-(C, Se)$_x$ environments assuming that the predominant $[SbSe_{3/2}]$ unit overlaps with the (Se)-Sb-C$_x$ etch products (Fig. 15c/d). Contrary to the Sb and Sb_2Se_3 sample, there is no Sb-Sb homopolar bond, which facilitates the interpretation of the spectra. However, the decomposition of the Sb

3d core level is also performed with the two Sb-(Se, C)$_x$ doublets at 529.0 eV (CS = 0.9 eV) and 529.7 eV (CS = 1.6 eV).

Two doublets are used to fit the Se 3d core level of the pristine thin film, which is composed of the (Se)-(Se)-(Ge, Sb) and Se-(Ge, Sb)$_2$ environments (Fig. 15e). It has been showed that the binding values of these two environments are influenced by the composition of the materials. After the CH_4/H_2/Ar etching, the Se 3d core level shifts to higher values, due to the bonding between selenium and the CH_x reactive neutral species (Fig. 15f). The spectrum is decomposed with two environments, whose dominant contribution centred at 54.7 eV is allocated to the C-Se-(Ge, Sb) species, then the doublet at higher values of binding energy corresponds to the (C)-Se-C environment (BE = 55.2 eV).

The decomposition of the Sb 4d / Ge 3d core levels mirrors those of the Ge $2p_{3/2}$ and Sb 3d so that the number of doublets in the Sb 4d/ Ge 3d region reflects the number of contributions in Ge $2p_{3/2}$ and Sb 3d core level. In the case of the pristine sample (Fig. 15g), its binding energy value (BE = 30.6 on Ge 3d) is lower than that of the $Ge_{31}Se_{69}$ thin film (see Fig. 12 and Table 1). Such disparity points out that the binding energy is likely affected by the [$SbSe_{3/2}$] motif. Then at the surface of the etched sample (Fig. 15h), the (Se)$_{4-x}$-Ge-C$_x$ $_x$ doublet is centered at 30.9 eV (CS = 1.9 eV), while [$SbSe_{3/2}$]a n d (Se)$_{3-x}$-Sb-(Se, C)$_x$ are positioned at 33.0 (CS = 1.1 eV) and 33.6 eV (CS = 1.7 eV), respectively. A large uncertainty of the surface quantification could arise from the overlapping between (Se)$_{4-x}$-Ge-C$_x$ and (Se)$_{3-x}$-Sb-(Se, C)$_x$ doublets.

	Ge $2p_{3/2}$				Ge $3d_{5/2}$			
	Pristine		Etched		Pristine		Etched	
	BE	FWHM	BE	FWHM	BE	FWHM	BE	FWHM
[$GeSe_{4/2}$]	1218.8	1.20			30.6	0.85		
(Se)-Ge-O	1220.3	1.47			32.0	0.88		
(Se)$_{4-x}$-Ge-C$_x$			1218.6	1.78			30.9	1.35

	Sb $3d_{5/2}$				Sb $4d_{5/2}$			
	Pristine		Etched		Pristine		Etched	
	BE	FWHM	BE	FWHM	BE	FWHM	BE	FWHM
[$SbSe_{3/2}$]	529.0	0.89	529.0	1.17	33.0	0.82	33.0	0.89
(Se)-Sb-O	529.8	2.01			34.1	1.52		
$(Se)_{3-x}$-Sb-$(Se, C)_x$			529.7	1.12			33.6	0.93

Table 4: Fit values extracted from Ge $2p_{3/2}$, Sb 3d, Se 3d and Sb 4d / Ge 3d XPS spectra (Fig. 15). *BE: Binding Energy (± 0.2 eV); FWHM: Full Width at Half Maximum (± 0.05 eV)*

Based on the XPS analysis of pure and binary materials, it can be concluded that methane-based etching processes deal inevitably with induced hydrocarbon etch products. These data on Ge-C, Sb-C, Se-C bonding (BE and FWHM) can be used to determine the rate limiting step of a methane-based etching process on binary or ternary material. Note that the change in surface composition should influence the optical and electrical performances of Ge-Se, Sb-Se and Ge-Sb-Se materials.

4. Conclusion

In this paper, plasma etching was used as an effective source of low m/z organometallic compounds and as an ionization method. Mass spectrometry analysis and MLR analysis were combined to introduce the $M_xH_y^+$ (M = Ge, Sb, Se), $M_xC_yH_z^+$ and $SeSbC_xH_y^+$ etch products during H_2/Ar and CH_4/H_2/Ar etching processes. So far, most of those compounds were exclusively detected during the fragmentation of stable organometallic compounds. In fact, the delimitation of the clusters is the only shared feature between our present study and the literature. We conclude that most of positive ions result from gas phase reactions rather than from dissociative ionization by electronic impact of stable organometallic compounds. Due to

the superposition of etch product signals, the identification of $M_xC_yH_z^+$ (M = Ge, Sb, Se) etch products was a mandatory step to interpret the $GeSe_2$ and Sb_2Se_3 MS spectra.

These MS data aim to facilitate the interpretation of MS spectra recorded during the etching of chalcogenide materials as Ge-Sb-Se, As-Sb-Se, Ge-Sb-Te and, to a lesser extent, the Ge-containing, Sb-containing (III-V semiconductors) and Se-containing (II-VI semiconductors) materials. More generally, the methodology could be extended for the interpretation of any MS spectra regardless of the material. From that perspective, MLR analysis is likely to open up many opportunities for organometallic investigations. If the CH_4/H_2/Ar etching process is applied to complex compounds (M_aM_b), gas phase reactions are expected to produce $M_aM_bC_xH_y^+$ ion clusters, as observed with the $SeSbC_xH_y^+$ clusters.

XPS analysis indicated a modification of the surface bonding after a methane-based plasma. On the Ge and Sb XPS spectra, the pronounced shifts to higher energy values were assigned to the (M)-M-C_x environments, resulting from the adsorption of -CH_x reactive neutrals or from redeposit of etch products. The pristine $Ge_{39}Se_{61}$, Sb_2Se_3 and $Ge_{19}Sb_{21}Se_{60}$ XPS spectra exhibited the [$GeSe_{4/2}$] and [$SbSe_{3/2}$] motifs. During the etching process, some of these structures are modified due to the presence of the M-C bonding. Such as, the induced etch products are the (Se)-M-Cx environments. Nevertheless, these entities and the dominant [$GeSe_{4/2}$] and [$SbSe_{3/2}$] units overlap, limiting greatly the interpretation. On the $Ge_{39}Se_{61}$ surface, the presence of the (Ge)-Ge-(C, Se)$_x$ entities is evidenced by a notable shift to lower value starting from the [$GeSe_{4/2}$] motif. Overall, all decomposed core levels were broadened due to the organometallic contributions. From another point of view, the identical electronegativity of Se and C could be exploited to investigate the hydrogen and methyl bonding of selenide materials. The identification of positive ions was a direct proof of an etching regime of the Ge-Se, Sb-Se and Ge-Sb-Se systems, despite the presence of nonvolatile

carbides at the surface. To that extend, the methane-based chemistry can be used for the etching of stoichiometric Ge-Se and Ge-Sb-Se systems. Further work is needed to evaluate the etching characteristics and the etched profile of such materials in a methane-based process.

ACKNOWLEDGMENTS

Czech Science Foundation (project no. 19-24516S) and the Barrande exchange program between France and the Czech Republic are greatly acknowledged for supporting this work.

REFERENCE

[1] Gadd G M 1993 *FEMS Microbiol. Rev.* **11** 297–316
[2] Bentley R and Chasteen T G 2002 *Microbiol. Mol. Biol. Rev.* **66** 250–271
[3] Craig P J and Jenkins R O 2004 Organometallic compounds in the environment: An overview *Organic Metal and Metalloid Species in the Environment: Analysis, Distribution, Processes and Toxicological Evaluation* ed Hirner A V and Emons H (Berlin, Heidelberg: Springer) pp 1–15
[4] Mason R P 2012 *Methylation - From DNA, RNA and Histones to Diseases and Treatment*
[5] Abbott J K C, Smith B A, Cook T M and Xue Z L 2017 Chapter 10 - Synthesis of Organometallic Compounds *Modern Inorganic Synthetic Chemistry (Second Edition)* ed Xu R and Xu Y (Amsterdam: Elsevier) pp 247–277
[6] Eller K and Schwarz H 1991 *Chem. Rev.* **91** 1121–1177
[7] Operti L and Rabezzana R 2006 *Mass Spectrom. Rev.* **25** 483–513
[8] Freiser B S 2012 *Organometallic Ion Chemistry* (Springer Science & Business Media)
[9] Henderson W and McIndoe J S 2005 *Mass Spectrometry of Inorganic and Organometallic Compounds: Tools - Techniques - Tips* (Wiley)
[10] Jiráskо R and Holčapek M 2011 *Mass Spectrom. Rev.* **30** 1013–1036
[11] Vikse K L and McIndoe J S 2018 *J. Mass Spectrom.* **53** 1026–1034
[12] Petkovi´c M and Kamˇceva T 2011 *Metallomics* **3** 550–565
[13] Krupp E M, Grümping R, Furchtbar U R R and Hirner A V 1996 *Fresenius J. Anal. Chem.* **354** 546–549
[14] Prange A and Jantzen E 1995 *J. Anal. At. Spectrom.* **10** 105–109
[15] Pearton S J and Ren F 1993 *J. Vac. Sci. Technol. B* **11** 15–19
[16] Chen W R, Chang S J, Su Y K, Lan W H, Lin A C H and Chang H 2000 *Jpn. J. Appl. Phys.* **39** 3308
[17] Semu A and Silverberg P 1991 *Semicond. Sci. Technol.* **6** 287
[18] Pearton S J, Hobson W S, Baiocchi F A and Jones K S 1990 *J. Electrochem. Soc.* **137** 1924–1934
[19] Pusino V, Xie C, Khalid A, Thayne I G and Cumming D R S 2016 *Microelectron. Eng.* **153** 11–14
[20] Vu K and Madden S 2011 *J. Vac. Sci. Technol. A* **29** 011023–011023
[21] Boulard F, Baylet J and Cardinaud C 2009
[22] Eddy C R, Leonhardt D, Shamamian V A and Butler J E 2001 *J. Electron. Mater.* **30** 538–542
[23] Melville D L, Simmons J G and Thompson D A 1993 *J. Vac. Sci. Technol. B* **11** 2038–2045
[24] Feurprier Y., Cardinaud C., Grolleau B., Turban G., 1997 Plasma Sources Sic. Technol. **6,** 561.
[25] Li J, Chen F, Shen X, Dai S x, Xu T f and Nie Q h 2015 *Optoelectron. Lett.* **11** 203–206
[26] Zhou J, Du Q, Xu P, Zhao Y, Lin R, Wu Y, Zhang P, Zhang W and Shen X 2018 *IEEE J. Sel. Top. Quantum Electron.* **24** 1–6
[27] Xiong H, Shi Y and Wang Z 2020 *Microelectron. Eng.* **225** 111259
[28] Baudet E, Cardinaud C, Boidin R, Girard A, Gutwirth J, Němec P and Nazabal V 2018 *J. Am.*

Ceram. Soc. **101** 3347–3356
[29] Shirley D A 1972 *Phys. Rev. B* **5** 4709–4714
[30] 1989 *X-ray Photoelectron Spectroscopy Database XPS,Version 4.1, NIST Standard Reference database 20* (National Institute of Standards and Technology)
[31] Ueno T 1983 *Jpn. J. Appl. Phys.* **22** 1349
[32] Mytilineou E, Kounavis P and Chao B S 1989 *J. Phys.: Condens. Matter* **1** 4687–4695
[33] Kandil K M, Kotkata M F, Theye M L, Gheorghiu A, Senemaud C and Dixmier J 1995 *Phys. Rev. B* **51** 17565–17573
[34] Theye M L, Gheorghiu A, Senemaud C, Kotkata M F and Kandil K M 1994 *Philosophical Magazine B* **69** *209-222 https://doi.org/10.1080/01418639408240104*
[35] Shiel H, Hutter O S, Phillips L J, Turkestani M A, Dhanak V R, Veal T D, Durose K and Major J D 2019 *J. Phys. Energy* **1** 045001 ISSN 2515-7655
[36] Kamruzzaman M, Liu C, Farid Ul Islam A K M and Zapien J A 2017 *Semiconductors* **51** 1615–1624
[37] Li Y, Zhou Y, Luo J, Chen W, Yang B, Wen X, Lu S, Chen C, Zeng K, Song H and Tang J 2016 *RSC Adv.* 6 87288–87293
[38] Laidani, N., Bartali, R., Tosi, P., & Anderle, M. 2004 Journal of Physics D: Applied Physics, 37(18), 2593–2606. doi:10.1088/0022-3727/37/18/016
[39] Bogaerts, R.Gijbels 2002 Spectrochimica Acta Part B 57 1071-1099
[40] Hjartarson, A. T., Thorsteinsson, E. G., & Gudmundsson, J. T. 2010 Plasma Sources Science and Technology, 19(6), 065008. doi:10.1088/0963-0252/19/6/065008
[41] Meyer T, LeDain G, Girard A, Rhallabi A, Bouška M, Němec P, Nazabal V and Cardinaud C, 2020 Plasma Sources Sci. Technol. **29,** 105006
[42] Saalfeld F 1961 *The mass spectra of some volatile hydrides* PhD Thesis Iowa State University
[43] van Der Kelen G P and van De Vondel D F 1960 *Bull. Soc. Chim. Belg.* **69** 504–516
[44] Operti L, Splendore M, Vaglio G A and Volpe P 1993 *Spectroc. Acta A* **49** 1213–1220
[45] Watanabe H, Yoshimura E, Taira T, Yamazaki S, Tsuchiya M and Toda S 1982 *Bunseki kagaku* **31** E273–E276
[46] Gudmundsson J T 1998 *Plasma Sources Sci. Technol.* **7** 330–336
[47] Jiménez-Redondo M, Cueto M, Doménech J L, Tanarro I and Herrero V J 2014 *RSC Adv.* **4** 62030–62041
[48] **X** R. C. Binning, Jr. L. A. Curtiss 1990 *J. Chem. Phys.* 92, 3688–3692
[49] W G Graham 1995 *Plasma Sources Sci. Technol.* **4** 281
[50] T Hjartarson, E G Thorsteinsson[2] and J T Gudmundsson *et al* 2010 *Plasma Sources Sci. Technol.* **19** 065008
[51] Tamaru K 1957 *J. Phys. Chem.* **61** 647–649
[52] Jo S K 2017 *Appl. Sci. Converg. Technol.* **26** 174–178
[53] A verifier !!!
[54] T. Nakano, H. Toyoda, H. Sugai 1991 *Jpn. J. Appl. Phys.* **30** 2908
[55] M. Stano, S. Matejcik, J. D. Skalny, T. D. Märk 2003 *J. Phys. B: At. Mol. Opt. Phys.* **36** 261
[56] Dibeler V H 1952 *J. Res. Natl. Inst. Stand. Technol.* **49** 235
[57] de Ridder J J and Dijkstra G 1967 *Recl. Trav. Chim. Pays-Bas* **86** 737–745
[58] Pinson J W and Khandelwal J K 1973 *Spectrosc. Lett.* **6** 745–761
[59] Greenlief C M and Klug D A 1992 *J. Phys. Chem.* **96** 5424–5429
[60] Jenkins R O, Craig P J, Goessler W, Miller D, Ostah N and Irgolic K J 1998 *Environ. Sci. Technol.* **32** 882–885
[61] Andrewes P, Cullen W R, Feldmann J, Koch I and Polishchuk E 1999 *Appl. Organomet. Chem.* **13** 681–687
[62] Koch I, Wang L, Feldmann J, Andrewes P, Reimer K and R Cullen W 2000 *Int. J. Environ. Anal. Chem.* **77** 111–131
[63] Andreae M O and P N 1984 *Tellus B* **36** 101–117
[64] Dodd M, A Pergantis S, R Cullen W, Li H, Eigendorf G K and J Reimer K 1996 *Analyst* **121** 223–228
[65] Feldmann J, Koch I and Cullen W R 1998 *Analyst* **123** 815–820
[66] Chau Y K, Wong P T S, Silverberg B A, Luxon P L and Bengert G A 1976 *Science* **192** 1130–1131

[67] Ranjard L, Prigent-Combaret C, Nazaret S and Cournoyer B 2002 *J. Bacteriol. Res.* **184** 3146– 3149
[68] Gabel-Jensen C, Lunøe K and Gammelgaard B 2010 *Metallomics* **2** 167–173
[69] Guo X, Sturgeon R E, Mester Z and Gardner G J 2003 *Appl. Organomet. Chem.* **17** 575–579
[70] Tsai J H, Hiserodt R D, Ho C T, Hartman T G and Rosen R T 1998 *J. Agric. Food Chem.* **46** 2541–2545
[71] Vilcarromero J, Marques F and Andreu J 1998 *J. Non-Cryst. Solids* **s 227-230** 427–431
[72] Wu X, Zhang W, Yan L and Luo R 2008 *Thin Solid Films* **516** 3189–3195
[73] Weightman P, Roberts E D and Johnson C E 1975 *J. Phys. C: Solid State Phys.* **8** 550–566
[74] Bahl M K, Watson R L and Irgolic K J 1980 *J. Chem. Phys.* **72** 4069–4077
[75] Orton B R, Saffarini G, Gorgol J and Rivière J C 1990 *Philosophical Magazine B* **62** 71–78 publisher: Taylor & Francis eprint: https://doi.org/10.1080/13642819008205535
[76] Powell C J and Jablonski A 2010 *NIST Electron Inelastic-Mean-Free-Path Database - Version 1.2* (National Institute of Standards and Technology, Gaithersburg, MD)
[77] Kotkata M F, El-Shair H T, Afifi M A and Abdel-Aziz M M 1994 *J. Phys. D: Appl. Phys.* **27** 623–627
[78] Vadapoo R, Krishnan S, Yilmaz H and Marin C 2011 *Phys. Status Solidi B* **248** 700–705
[79] Chang-Yong Z, Li-Wu W and Ning-Kang H 2007 *Chinese Phys. Lett.* **24** 803
[80] Mahmood A, Shah A, Castillon F F, Araiza L C, Heiras J, Akhtar Raja M Y and Khizar M 2011 *Curr. App. Phys.* **11** 547–550
[81] Golovchak R, Shpotyuk O, Kozyukhin S, Kovalskiy A, Miller A C and Jain H 2009 *Journal of Applied Physics* **105** 103704 ISSN 0021-8979
[82] Hohl D, Jones R O, Car R and Parrinello M 1987 *Chem. Phys. Lett* **139** 540–545
[83] Goldan A H, Li C, Pennycook S J, Schneider J, Blom A and Zhao W 2016 *J. Appl. Phys.* **120** 135101
[84] Baudet E, Cardinaud C, Girard A, Rinnert E, Michel K, Bureau B and Nazabal V 2016 *Journal of Non-Crystalline Solids* **444** 64–72
[85] Wei W H, Xiang S, Xu S W, Fang L and Wang R P 2014 *Journal of Applied Physics* **115** 183506
[86] Chen Y, Shen X, Wang R, Wang G, Dai S, Xu T and Nie Q 2013 *Journal of Alloys and Compounds* **548** 155–160 ISSN 0925-838